Journal of Translational Medicine

RESEARCH

Open Access

Au@Pd nanozyme-mediated catalytic therapy: a novel strategy for targeting tumor microenvironment in cancer treatment

Min Luo[1], Fu-kun Zhao[1], Yuan-min Wang[1] and Jiang Bian[2,3*]

Abstract

Background Breast cancer, with its high morbidity and mortality rates, is a significant global health burden. Traditional treatments—surgery, chemotherapy, and radiotherapy—are widely used but come with drawbacks such as recurrence, metastasis, and significant side effects, including damage to healthy tissues. To address these limitations, new therapeutic strategies are being developed. Peroxidases (POD) can catalyze excess H_2O_2 in the tumor microenvironment to generate reactive oxygen species (ROS), which induce cancer cell apoptosis by disrupting redox homeostasis and modulating apoptosis-related proteins. However, natural enzymes face challenges like poor stability, high cost, and sensitivity to environmental conditions, limiting their application in breast cancer treatment. Nanozymes, nanomaterials with enzyme-like activity, offer a promising alternative by overcoming these limitations.

Methods In this study, we successfully prepared Au@Pd nanozymes with peroxidase activity by depositing metallic Pd on Au nanoparticles (Au NPs) synthesized using a trisodium citrate reduction method and ascorbic acid reduction. The in vitro validation was conducted through a series of experiments, including ROS detection, flow cytometry, CCK-8 assay, DNA damage assessment, live/dead cell staining, Western blot (WB), and qPCR. Tumor treatment was performed via tail vein injection of the drug, followed by HE staining of the treated tissues and biochemical analysis of the blood.

Results Au@Pd nanozymes can effectively accumulate at the tumor site through the EPR effect and exert peroxidase-like activity, catalyzing the excess H_2O_2 in the tumor microenvironment to produce ROS. This triggers apoptosis pathways and DNA damage, leading to the downregulation of the anti-apoptotic protein Bcl-2, upregulation of the pro-apoptotic protein Bax, and induction of apoptosis-related genes, demonstrating strong anti-tumor effects.

Conclusions This study developed an efficient nanozyme-mediated catalytic therapy strategy targeting the tumor microenvironment for the treatment of breast cancer cells.

Keywords Catalytic therapy, Tumor, Peroxidases, Nanozymes

*Correspondence:
Jiang Bian
19707763798@163.com
[1]The Third Affiliated Hospital of Zunyi Medical University, The First People's Hospital of Zunyi, Zunyi, Guizhou 563000, China
[2]Dali University, No.2 Hongsheng Road, Dali Town, Dali City 671003, Yunnan Province, China
[3]Department of anesthesiology, Panzhihua central hospital, No.34 Yikang Street, East District, Panzhihua City 617000, Sichuan Province, China

Introduction

The regulation of growth, proliferation, differentiation, senescence, and death in cells of living organisms are all regulated by strict genetic programming. Under normal circumstances, cells typically undergo approximately 50 generations of proliferation before undergoing programmed cell death [1]. However, genetic mutations or exposure to environmental factors such as radiation and pollution can disrupt this regulatory process, leading to uncontrolled growth and division of cells, known as cancer cells [2]. The tireless proliferation and replication of cancer cells significantly disrupt the regular processes of cell growth, division, and senescence. As cancer cells proliferate and divide, they progressively depart from their normal physiological state, exhibiting increased proliferation rates, heightened resistance to regulatory mechanisms of normal tissue, and eventual breach of tissue boundaries leading to metastasis [3].

According to the latest report from the International Agency for Research on Cancer (IARC) of the World Health Organization in 2024, there were an estimated 20 million new cancer cases and 9.7 million cancer-related deaths worldwide in 2022 [4]. Approximately 53.5 million individuals survive five years post-cancer diagnosis. Globally, about one in five people is affected by cancer, with mortality rates of one in 12 for women and one in 9 for men [5, 6]. The incidence of breast cancer, in particular, has seen a troubling rise, with significant geographic and socioeconomic disparities in outcomes. Breast cancer is the most common malignancy among women worldwide, accounting for a substantial portion of cancer cases. It is estimated that one in eight women will be diagnosed with breast cancer during their lifetime [7, 8]. This disease is heterogeneous, encompassing multiple subtypes with different biological behaviors and responses to treatment. Despite advances in early detection and treatment strategies, breast cancer remains a leading cause of cancer-related morbidity and mortality globally.

In 1600 BCE, the Edwin Smith Papyrus described eight cases of breast and uterine cancer [9]. In the Middle Ages, Johannes Scultetus used primitive mastectomy methods involving burning, acid, and binding. In the 1890s, William Stewart Halsted of Johns Hopkins University developed the radical mastectomy, which removed the breast, underlying muscles, and lymph nodes [10]. Despite advancements in anesthesia and aseptic techniques, surgery's limitations, including metastasis, recurrence, and reduced survival rates, persist [11]. Radiotherapy, originating from Roentgen's 1895 discovery of X-rays and the Curies' 1898 discovery of radium (Ra), can effectively destroy tumors but also damage healthy cells, necessitating precise tumor-targeting techniques [12]. Chemotherapy began with World War II's nitrogen mustard and now includes drugs like cisplatin [13], carboplatin [14], and Adriamycin [15], but these treatments cause severe side effects such as cardiotoxicity and neurotoxicity. Initially, many patients chose to end their lives due to the intense suffering from chemotherapy and radiotherapy, highlighting the urgent need for more effective cancer treatments.

With the onset of the 21st century, advancements in science and technology, particularly in life sciences and nanotechnology, have led to novel cancer treatment modalities. Among these, therapies generating reactive oxygen species (ROS) to induce tumor cell death have emerged. For example, photodynamic therapy (PDT) uses light to activate photosensitizers (PS) to produce toxic ROS, though it is limited to superficial tumors due to light penetration constraints [16]. Sonodynamic therapy (SDT), with deeper tissue penetration, activates sonosensitizers under ultrasound to produce ROS and kill tumors [17]. In 2007, Chinese scientists synthesized peroxidase-active Fe_3O_4, catalyzing H_2O_2 to produce biotoxic ROS in the acidic tumor microenvironment [18]. ROS are highly toxic, causing oxidative damage and inducing cell apoptosis. Fe_3O_4, a nanozyme, offers advantages over natural enzymes, including similar catalytic activity, low production cost, long storage time, and easier transportation [19, 20]. This breakthrough paved the way for using inorganic nanoparticles as biologically active enzymes, gaining global attention [21, 22]. Subsequently, nanoparticles with various biological enzyme activities have been synthesized and reported, highlighting their potential in cancer treatment [23, 24].

The common types of nanozymes reported in current studies mainly include noble metal nanozymes, metal-organic frameworks (MOF), metal-based oxides, and transition metal-containing biomolecules [25–27]. Among them, Aurum (Au) [28, 29], palladium (Pd) [30–32], platinum (Pt) [33, 34], iridium (Ir) [35] and rhodium (Rh) [36] are the main components of noble metal nanozymes, which can directly combine with organic small molecules, biological molecules (nucleic acids, peptides, antibodies, etc.) or other materials (MOFs, carbon nanotubes, etc.). In addition, two or more noble metals can combine with each other to form an alloy, and the formed alloy has better catalytic activity than a single noble metal enzyme [37, 38].

We have successfully synthesized alloy nanozymes (Au@Pd) containing two precious metals, Aurum (Au) and palladium (Pd). Au@Pd nanozymes have the advantages of small nanoparticle diameter and high peroxidase activity. Au@Pd nanozymes can catalyze excess H_2O_2 to generate cytotoxic ROS in the acidic tumor microenvironment, disrupt intracellular redox homeostasis, and activate proteins related to mitochondrial apoptosis pathway to induce tumor cell apoptosis, which has

great potential in the catalytic application of nanozymes. Additionally, the Au@Pd nanozymes exhibit higher Km and Vmax values compared to HRP and Au NPs, suggesting that the synthesized Au@Pd nanozymes have great potential to replace natural HRP in catalytic cancer therapy.

Results

Synthesis and characterization of au NPs and Au@Pd nanozymes

Following the synthesis of Au nanoparticles via trisodium citrate reduction, Au@Pd nanozymes were fabricated through the reduction of ascorbic acid and the subsequent deposition of palladium metal onto the Au nanoparticle surfaces (Fig. 1A). In this investigation, TEM, SEM, and EDS analyses were employed to visually and accurately discern the morphological characteristics and elemental composition of the Au NPs and Au@Pd nanozymes. Figure 1B and C illustrate that the Au NPs and Au@Pd nanozymes produced by this method exhibit a spherical shape, uniform size, and excellent dispersibility. The EDS spectrum clearly indicates the presence of both gold (Au) and palladium (Pd) elements in the synthesized Au@Pd nanozymes, with the yellow hue representing Pd elements appearing more vibrant and exhibiting a broader distribution than the orange hue representing Au elements (Fig. 1D). In the UV-vis spectrum, Au NPs display a distinct absorption peak at 520 nm; however, this peak vanishes upon Pd coating, and the solution color transitions from burgundy to brown (Fig. 1E). This observation aligns with the elemental mapping results, confirming the growth of Pd shells on Au NPs and their uniform distribution. Particle size measurements of Au NPs and Au@Pd nanozymes were conducted using DLS. The diameter of Au NPs is approximately 15 nm, signifying a concentrated size distribution with minimal presence of large by-product particles (Fig. 1F). Employing Au NPs as precursors, the synthesized Au@Pd nanozymes nanoparticles exhibit a size of 20 nm (Fig. 1G). To further elucidate the charge properties of Au NPs and Au@Pd nanozymes, their zeta potentials were characterized. As shown in Fig. 1H, Au NPs possess a negative surface charge of approximately −18 mV, while the Pd-shell-coated Au@Pd nanozymes maintain a negative charge of about −10 mV. This disparity in charged characteristics substantiates the successful coating of Pd shells onto Au NPs to create Au@Pd nanozymes.

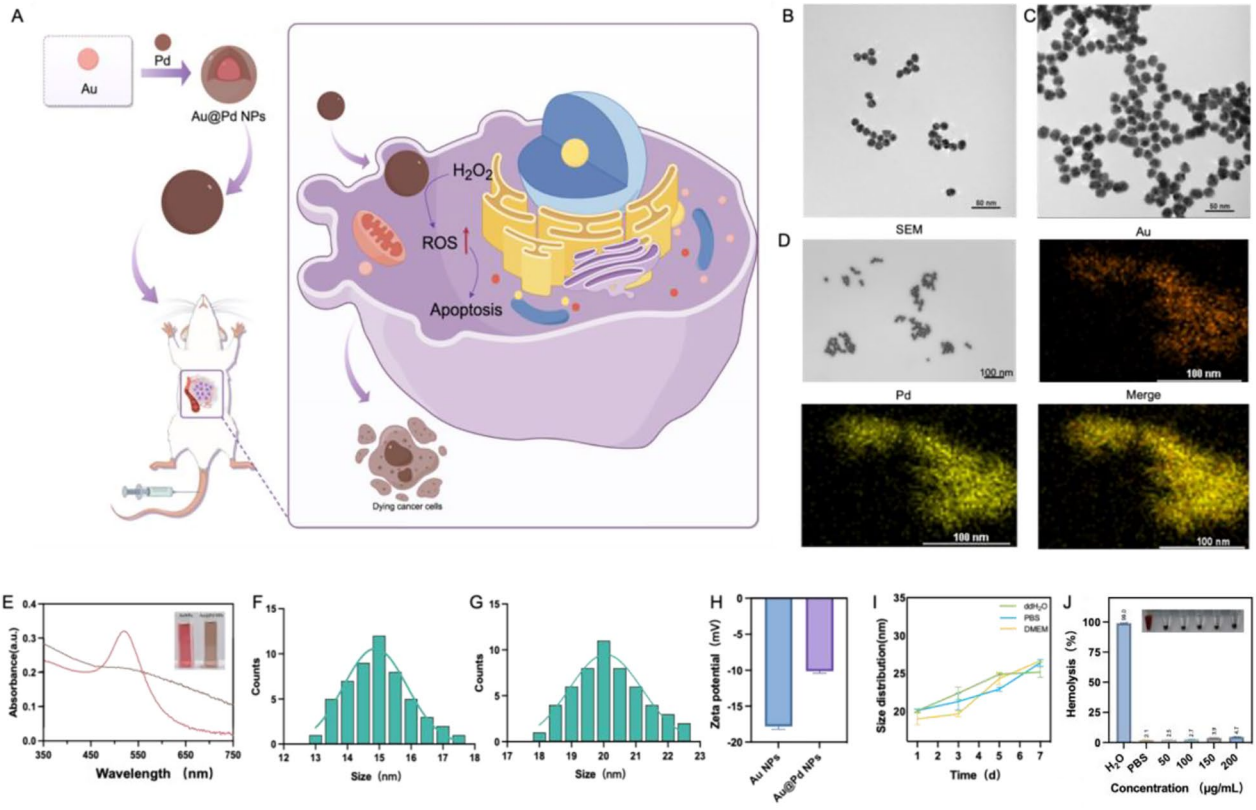

Fig. 1 **(A)** Synthesis of Au@Pd NPs. **(B)** TEM images of Au NPs; **(C)** TEM images of Au@Pd nanozymes; **(D)** SEM images and EDS of Au@Pd nanozymes; **(E)** UV – vis absorption spectra of Au NPs and Au@Pd nanozymes; **(F-G)** Hydrodynamic diameters of AuNPs and Au@Pd nanozymes; **(H)** Zeta potential of Au NPs and Au@Pd nanozymes; **(I)** Particle size stability of Au@Pd Nanozymes; **(J)** Hemolysis rate of Au@Pd Nanozymes

Analysis of particle size stability and hemolysis rate of Au@Pd nanozymes

The stability of the nanomaterials' particle size was examined by immersing them in various solutions. Specifically, we assessed the Au@Pd Nanozymes' particle size in ddH_2O, PBS, and DMEM supplemented with 10% FBS over a span of seven days. As demonstrated in Fig. 1I, the Au@Pd Nanozymes' particle size remained relatively stable at approximately 20–25 nm in all three media, indicating favorable stability. In addition, we evaluated the hemolysis rate of Au@Pd Nanozymes to ensure their biosafety. Fresh blood was collected from mice via orbital blood sampling and exposed to diluted Au@Pd Nanozymes in PBS. As shown in Fig. 1J, the hemolysis rates of the Au@Pd Nanozymes exhibited negligible differences between the concentrations of 50 μg/mL and 200 μg/mL. PBS-treated group and ddH_2O-treated group were also incorporated as negative and positive controls, respectively. The results revealed that the PBS-treated group's hemolysis rate was comparable to the experimental group's, while the absorbance of the ddH_2O-treated group significantly surpassed the other groups.

Identification of Au@Pd nanozymes with peroxidase activity

The peroxidase activity of Au@Pd nanozymes was investigated by measuring the TMB and H_2O_2 reaction system's absorbance intensity (Fig. 2A). The results demonstrated that the oxidation of colorless TMB to blue oxTMB by H_2O_2 was accelerated by Au@Pd Nanozymes as a catalyst. This catalytic process resulted in a dark blue color in the reaction system, which was approximately three times higher than the response signal of the simple Au@Pd nanozymes and H_2O_2 curve, confirming the peroxidase activity of Au@Pd nanozymes (Fig. 2B).

To achieve optimal peroxidase catalytic activity, the TMB and H_2O_2 reaction system's key analytical parameters were fine-tuned, including the pH value of the reaction medium HAc-NaAc buffer, the H_2O_2 concentration, and the TMB concentration. Figure 2C shows the

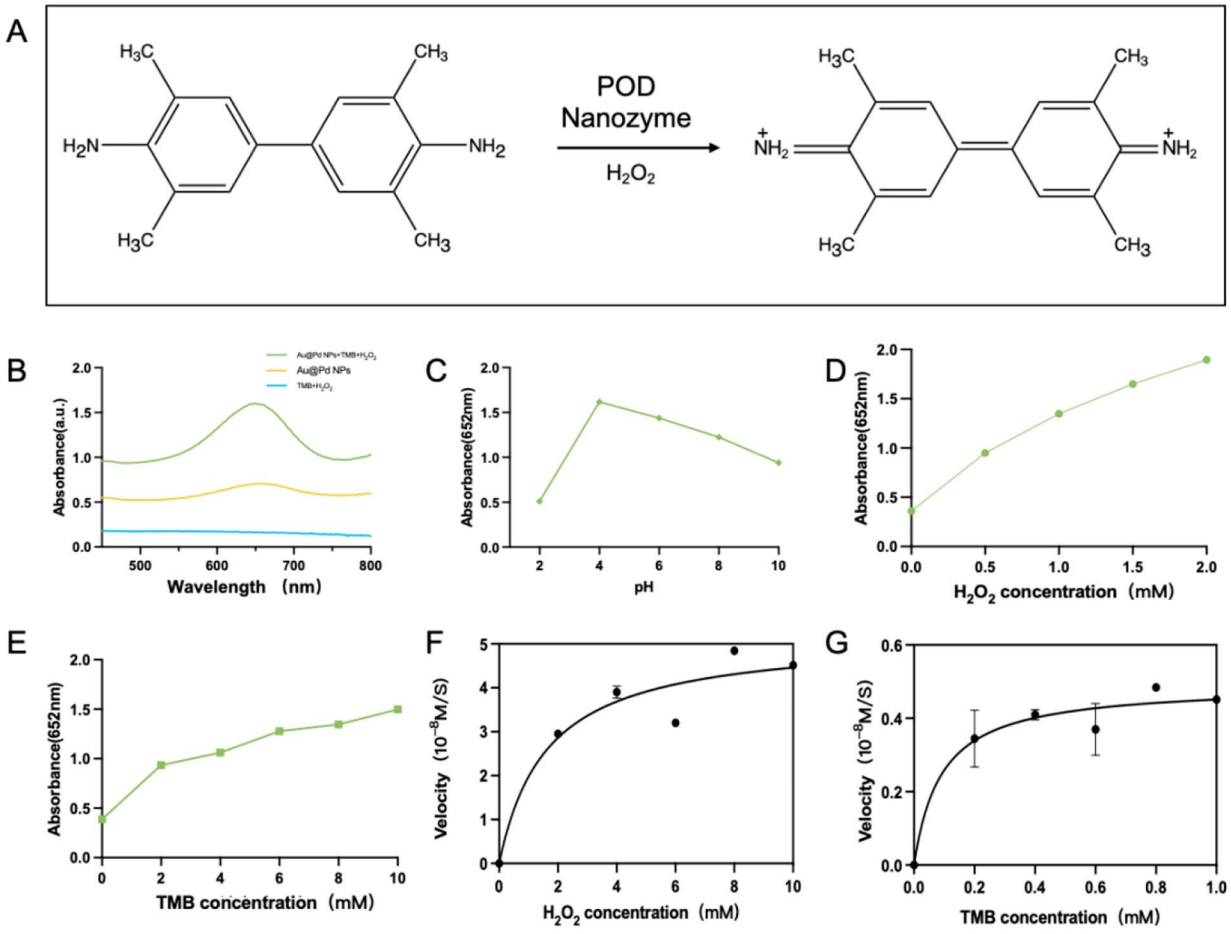

Fig. 2 **(A)** TMB classic color principle; **(B)** Absorbance and color development of different treatment groups; **(C)** Absorbance curves at different pH values; **(D)** Absorbance curves under different H_2O_2 conditions; **(E)** Absorbance change curves under different TMB. Steady-state kinetic analysis of Au@Pd nanozymes for H_2O_2**(F)** and TMB **(G)** using Michaelis-Menten

peroxidase catalytic activity of Au@Pd nanozymes under different pH values. The results revealed that the catalytic performance of Au@Pd Nanozymes was pH-dependent, exhibiting a green color under strongly acidic conditions (pH=2), and a light blue color under weakly alkaline conditions (pH=6–10). The optimal enzymatic activity of Au@Pd nanozymes was observed at pH=4, where the reaction solution was dark blue [39, 40].

Further exploration of the relationship between the peroxidase activity of Au@Pd nanozymes and different concentrations of H_2O_2 and TMB was conducted. The results showed that the absorbance value of oxTMB at 652 nm increased with the concentration of H_2O_2 and TMB within 200 s of the initial reaction (Fig. 2D and E), indicating a significant concentration dependence for the peroxidase activity of Au@Pd nanozymes.

Kinetic analysis of the enzymatic reaction of Au@Pd nanozymes

After establishing the pH and concentration dependence of the peroxidase activity of Au@Pd nanozymes, the steady-state kinetic parameters, such as Michaelis constant (K_m) and maximum reaction velocity (V_{max}), were determined to further investigate the enzymatic reaction kinetics. The Michaelis equation was established, and the K_m and Vmax values of Au@Pd nanozymes were obtained using H_2O_2 and TMB as substrates.

As shown in Fig. 2F and G, the K_m and V_{max} values of Au@Pd nanozymes were obtained when H_2O_2 and TMB were used as substrates, respectively. The results showed that the K_m and V_{max} values of Au@Pd nanozymes were 9.220 mM and 3.619×10^{-6} Ms^{-1}, respectively, when H_2O_2 was used as the reaction substrate. When TMB was the reaction substrate, the K_m value of Au@Pd nanozymes was 2.082 mM, and the V_{max} value was 4.95×10^{-6} Ms^{-1}. In addition, for TMB or H_2O_2 substrate, Au@Pd nanozymes of Km are slightly higher than the natural HRP, Vmax is far higher than the HRP and Au NPs, which makes the preparation of Au@Pd nanozymes have great potential to replace natural HRP TMB catalytic oxidation, achieve more catalytic treatment of cancer [41]. These results indicate that the Au@Pd nanozymes exhibit enzymatic kinetics characteristics, which can be further studied and applied in various fields.

Cellular uptake of Au@Pd nanozymes

Prior to the application of nanomaterials in medical biology, the critical factor for the therapeutic efficacy of nanomaterials is to ascertain whether they can be internalized by cells. To this end, we conducted ultrathin sectioning and transmission electron microscopy (TEM) imaging after co-incubating Au@Pd nanozymes with 4T1 cells for 8 h. As depicted in Fig. 3A and B, following 12 h of co-incubation, Au@Pd nanozymes were observed to be efficiently taken up and internalized by 4T1 cells

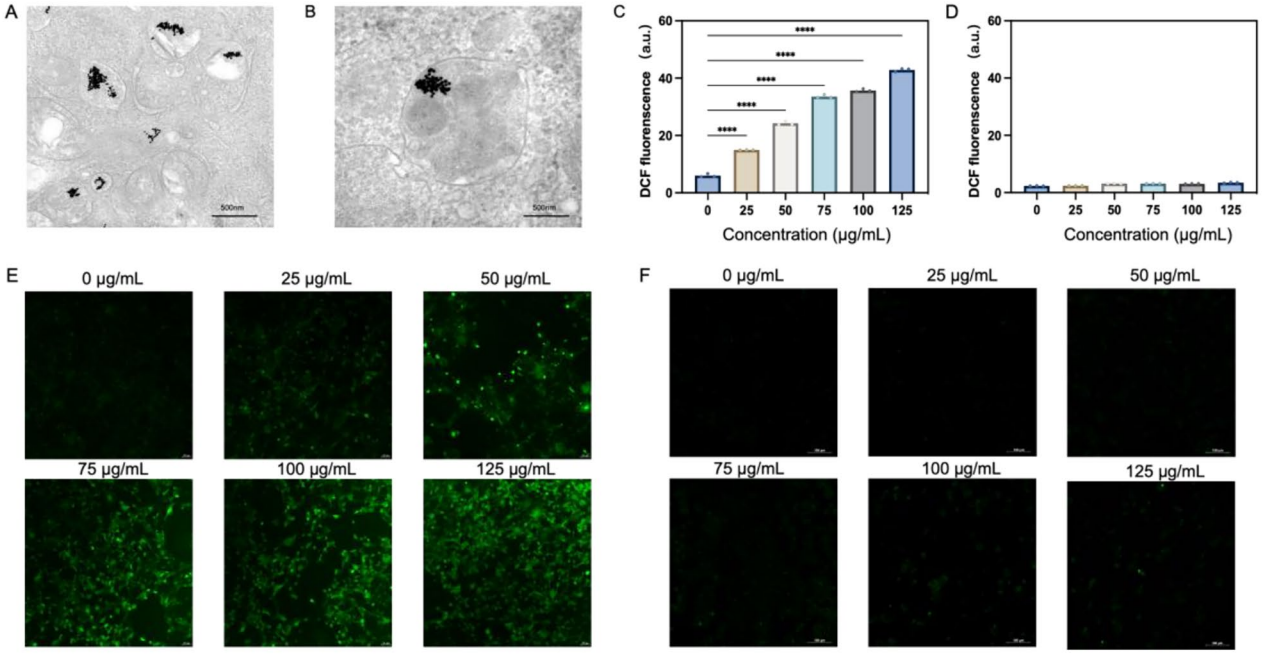

Fig. 3 **(A-B)** TEM images of uptake of Au@Pd nanozymes by 4T1 cells; (**C** and **E**) Quantification of ROS levels produced by 4T1 and HC11 treated with different concentrations of Au@Pd nanozymes; (**D** and **F**) Fluorescence images of ROS levels produced by 4T1 and HC11 cells treated with different concentrations of Au@Pd nanozymes. $^{***}P<0.001$

under TEM and were predominantly localized in the cytoplasm. This finding indicates that Au@Pd nanozymes can be readily internalized by tumor cells, which is a crucial prerequisite for their potential therapeutic applications in cancer treatment.

ROS generation

After confirming the stability, peroxidase activity, and cellular uptake of Au@Pd nanozymes, we further investigated their impact on reactive oxygen species (ROS) production in cells. Specifically, we used the DCFH-DA probe to assess the ROS generation in 4T1 cells after treatment with Au@Pd nanozymes with peroxidase activity. Our results revealed that compared to the faint green fluorescence observed in the control group, the ROS fluorescence intensity in 4T1 cells treated with 25 μg/mL Au@Pd nanozymes was significantly enhanced (Fig. 3C and E). Furthermore, the ROS fluorescence intensity increased progressively with the increase in the concentration of Au@Pd nanozymes, with the highest intensity observed at a concentration of 125 μg/mL. This result suggests that Au@Pd nanozymes with peroxidase activity can effectively catalyze the production of ROS with higher cytotoxicity in 4T1 cells.

Interestingly, when HC11 cells were treated with Au@Pd nanozymes, the ROS fluorescence was minimal, and only weak fluorescence was detected in the 125 μg/mL Au@Pd nanozymes treatment group (Fig. 3D and F). This finding can be attributed to the low H_2O_2 content in normal cells, which is insufficient to trigger the catalytic production of ROS by Au@Pd nanozymes. Therefore, our results demonstrate that Au@Pd nanozymes exhibit an excellent ability to generate ROS in tumor cells, which is a crucial factor for their potential therapeutic applications in cancer treatment.

Staining of live and dead cells

To visualize and clearly assess the therapeutic effect of Au@Pd nanozymes against 4T1 cells, calcein-AM (green fluorescence) and propidium iodide (PI) (red fluorescence) were used to stain 4T1 cells and HC11 cells, respectively. As shown in Fig. 4A, nearly all tumor cells in the control group of 4T1 cells remained viable, as indicated by the green fluorescence. The appearance of red fluorescence in 4T1 cells treated with 25 μg/mL Au@Pd nanozymes suggested that apoptosis was induced following co-incubation with these nanozymes. With increasing concentrations of Au@Pd nanozymes, the red fluorescence intensity gradually intensified, reaching a peak at 125 μg/mL. This demonstrated that Au@Pd nanozymes were capable of catalyzing the production of ROS from H_2O_2 in 4T1 cells and effectively promoting cell apoptosis, which was in agreement with the previous findings.

In contrast, when Au@Pd nanozymes were incubated with HC11 cells, the red fluorescence in the 25 μg/mL Au@Pd nanozymes treatment group, the 50 μg/mL Au@Pd nanozymes treatment group, and the 75 μg/mL Au@Pd NP treatment group was barely detectable. Only a faint red fluorescence was observed when the concentration of Au@Pd nanozymes reached 100 μg/mL, and the red fluorescence remained weak in the 125 μg/mL Au@Pd nanozymes-treated group (Figure S1). This indicates that Au@Pd nanozymes were less effective in inducing apoptosis in normal cells.

DNA damage

In line with our previous research, Au@Pd Nanozymes with peroxidase functionality induced cancer cell demise indirectly by leveraging the excessive H_2O_2 in tumor cells to generate ROS in large quantities. DNA damage, a crucial step in this process, primarily affects the double helix structure. To delve deeper into the therapeutic effect of the peroxidase activity in Au@Pd Nanozymes, we examined the DNA damage levels in 4T1 and HC11 cells subjected to various concentrations of these nanozymes. γ-H2AX, a well-established marker for double-strand DNA breaks, was employed to visualize the damage in cells treated with Au@Pd Nanozymes. The control 4T1 cells displayed minimal green fluorescence, indicating undamaged DNA (Fig. 4B). The DNA damage in cancer cells escalated in a dose-dependent manner as the concentration of Au@Pd Nanozymes increased. Moreover, upon nuclear staining with DAPI, the overlapping blue fluorescence indicating the nucleus and the green fluorescence indicating DNA damage confirmed that the damage occurred predominantly within the nucleus.

Subsequently, we investigated the extent of DNA damage in human normal HC11 cells induced by Au@Pd Nanozymes. The control and treated cells exhibited negligible green fluorescence signals (Figure S2), reinforcing the notion that the peroxidase activity of Au@Pd Nanozymes is essential for DNA damage and cell death, as it requires elevated levels of H_2O_2. Under normal H_2O_2 conditions, these nanozymes do not provoke DNA damage or apoptosis in normal cells, aligning with our previous observations.

Western blot

In normal physiological conditions, the anti-apoptotic protein Bcl-2 resides on the outer mitochondrial membrane, inhibiting the release of cytochrome c. Meanwhile, pro-apoptotic protein Bax remains in the cytoplasm as a monomer. Upon receiving apoptotic signals, Bax translocates to mitochondria and forms multimeric pores, facilitating cytochrome c release. Subsequently, cytochrome c binds to the apoptotic protease activating factor Apaf-1 and caspase-9, forming an activation complex that

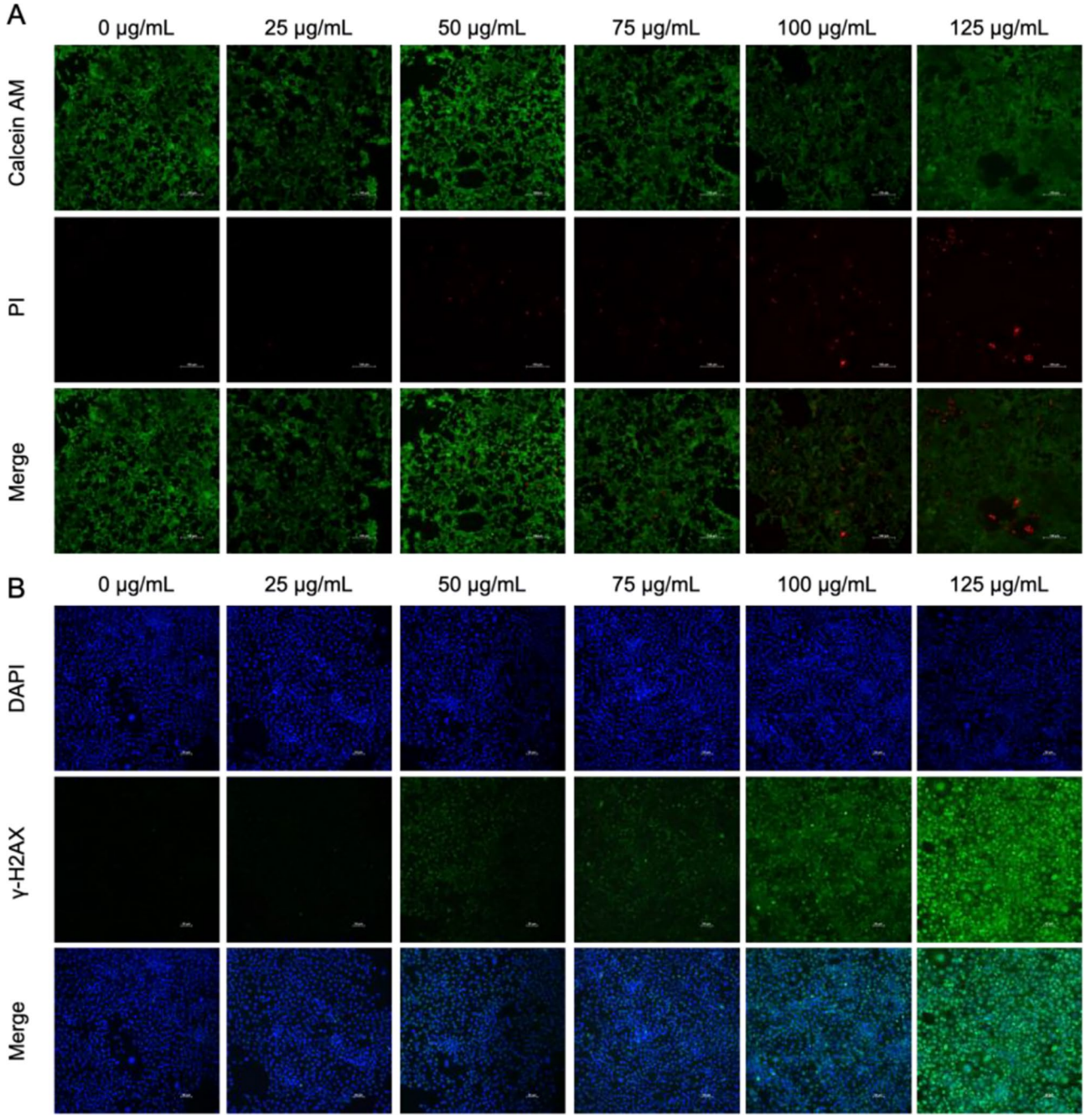

Fig. 4 **(A)** Fluorescence images of live and dead cells in 4T1 cells treated with different concentrations of Au@Pd nanozymes; **(B)** Fluorescence images of DNA damage in 4T1 cells treated with different concentrations of Au@Pd nanozymes

triggers caspase-9 activation. Activated caspase-9 then activates downstream caspase effector proteins, such as caspase-3 and caspase-7, to execute the apoptotic program. Additionally, DNA damage, a hallmark of apoptosis, activates p53.

Given these previous findings, Au@Pd nanozymes with peroxidase activity indirectly induce tumor cell apoptosis by catalyzing H_2O_2 to produce ROS in 4T1 cells. We confirmed the ROS-triggered apoptotic pathway induced by Au@Pd nanozymes through western blot analysis of apoptosis-related protein gene expression (Fig. 5A). compared to the control group, Apaf-1 expression was significantly upregulated in all experimental groups ($P<0.001$). As the concentration of Au@Pd nanozymes increased, pro-regulatory protein Bax expression was upregulated, exhibiting a significant correlation with the control group ($P<0.001$). Meanwhile, anti-apoptotic protein Bcl-2 expression in experimental groups gradually decreased,

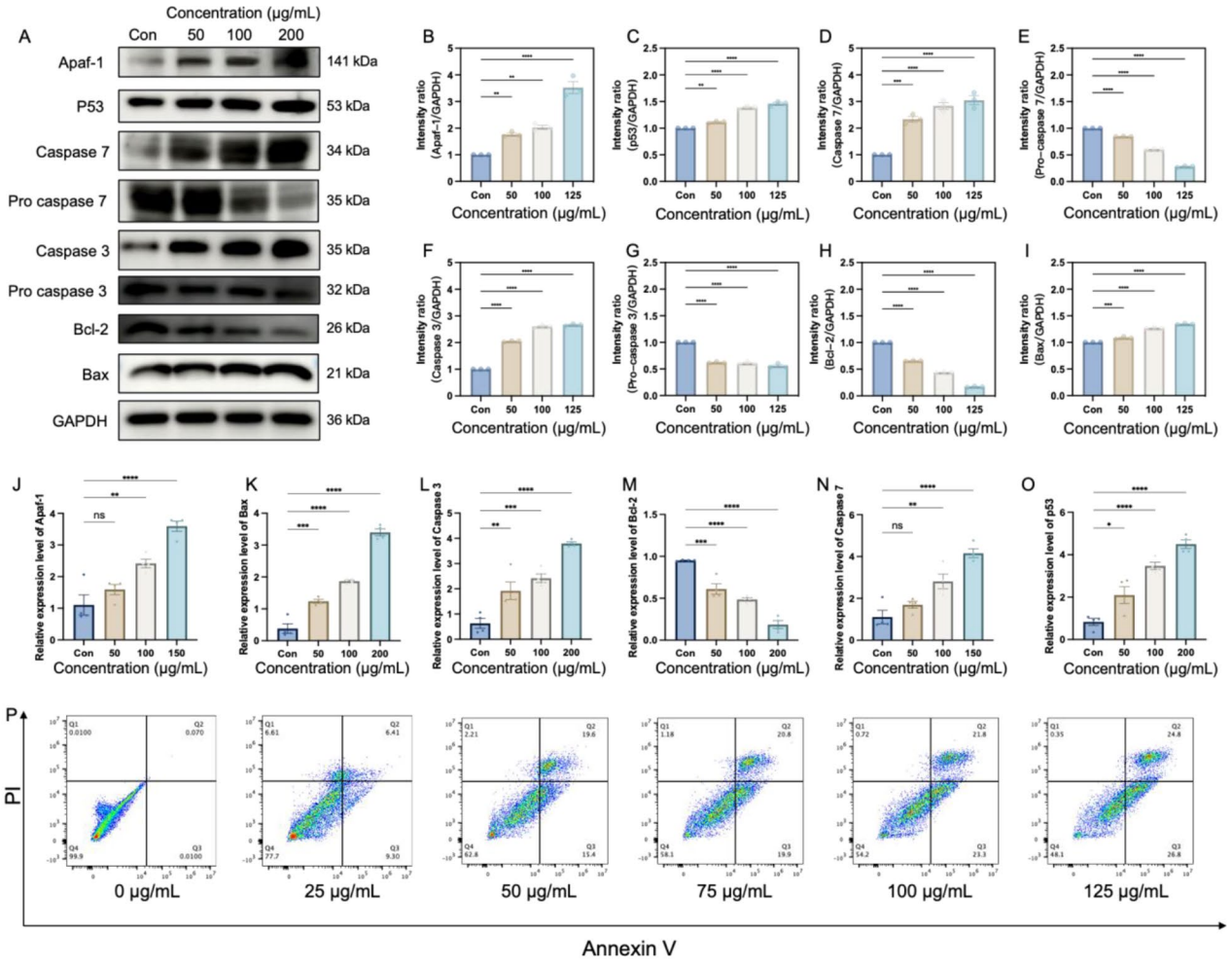

Fig. 5 **(A)** The expression of apoptosis-related proteins in 4T1 cells treated with different concentrations of Au@Pd nanozymes was detected by WB; **(B-I)** Panel A quantitative analysis of the corresponding proteins ($n=3$). **(J-O)** The expression of apoptosis-related proteins in 4T1 cells treated with different concentrations of Au@Pd nanozymes was detected by RT-PCR ($n=3$); **(P)** Flow cytometric analysis of apoptosis of 4T1 cells treated with different concentrations. $^{**}P<0.01$; $^{***}P<0.001$; $^{****}P<0.0001$

displaying a strong dose dependence ($P<0.001$). Concurrently, caspase-3 and caspase-7 expression was progressively increased with the onset of apoptosis ($P<0.001$). Furthermore, pro-caspase-3 and pro-caspase-7 expression significantly decreased in a dose-dependent manner, promoting 4T1 cell apoptosis. Additionally, p53 expression was elevated in 4T1 cells compared to controls, indicating that Au@Pd nanozymes upregulated p53 levels (Fig. 5B-I). In summary, these results suggest that Au@Pd nanozymes promote 4T1 cell apoptosis by regulating p53 and apoptosis-related signals.

Real-time fluorescence quantitative PCR

The western blot (WB) results revealed that Au@Pd nanozymes induced apoptosis in 4T1 cells. To further investigate the impact of Au@Pd nanozymes on apoptosis-related RNA in 4T1 cells, we performed quantitative polymerase chain reaction (qPCR) analysis. qPCR results corroborated the WB findings, demonstrating high expression of Bax, caspase-3, caspase-7, and p53, as well as low expression of Bcl-2, as the concentration of Au@Pd nanozymes increased (Fig. 5J-O). These consistent results further support the role of Au@Pd nanozymes in promoting 4T1 cell apoptosis through the regulation of apoptosis-related signals, including Bax, caspases, and p53.

Detected of tumor cells apoptosis

To intuitively quantify the rate of apoptosis, we employed Annexin V/propidium iodide (PI) co-staining to assess 4T1 and HC11 cells treated with various concentrations of Au@Pd nanozymes. The flow cytometry results clearly illustrate that the apoptosis rate of 4T1 cells in the control group was merely 0.1% (Fig. 5P). This rate progressively increased with the elevation of Au@Pd nanozymes concentration. Notably, when the concentration of Au@

Pd nanozymes reached 100 μg/mL and 125 μg/mL, the apoptosis rates of the tumor cells were elevated to 45.8% and 51.9%, respectively. These findings are in harmony with the outcomes of live/dead cell staining.

In parallel, the flow cytometry analysis of HC11 cells exposed to different concentrations of Au@Pd nanozymes yielded negligible apoptosis rates in the 25 μg/mL, 50 μg/mL, and 75 μg/mL treatment groups. However, when HC11 cells were treated with 100 μg/mL Au@Pd nanozymes for 24 h, the apoptosis rate reached 15.7%. Increased to 29.9% was the apoptosis rate observed in HC11 cells treated with 125 μg/mL Au@Pd nanozymes (Figure S3). These data collectively demonstrate a concentration-dependent pro-apoptotic effect of Au@Pd nanozymes on both 4T1 and HC11 cell lines, with 4T1 cells being more sensitive to the treatment at higher concentrations.

CCK-8 assay detected cell proliferation

Considering the promising peroxidase-like catalytic activity of Au@Pd Nanozymes and the abundant H_2O_2 in tumors, these nanozymes hold potential as therapeutic agents for treating tumors, both in vivo and in vitro. To further investigate their cytotoxicity, we conducted a CCK-8 assay on 4T1 cells and HC11 cells. Our results show that the cytotoxicity of Au@Pd Nanozymes increases with higher concentrations and longer incubation times (Figure S4A-S4D). Specifically, 4T1 cells exhibit dose-dependent cytotoxicity, while HC11 cells treated with the same dose and time show no significant cytotoxicity (Figure S4E-S4H).

In summary, Au@Pd nanozymes exhibit cytotoxic effects only in tumor cells with excess H_2O_2 in a dose-dependent manner, while causing minimal harm to normal cells. These findings suggest that Au@Pd nanozymes could be a promising and selective therapeutic strategy for tumors, warranting further investigation.

In vivo therapy

Based on the impressive therapeutic outcomes of Au@Pd nanozymes at the cellular level and their favorable biosafety profile, we further examined the tumor growth inhibition efficacy of Au@Pd nanozymes through in vivo treatment. Following the development of the 4T1 tumor model and randomization, 100 μL of varying concentrations of Au@Pd nanozymes or PBS were administered via tail vein injections on days 0, 2, and 4. Tumor volume and mouse body weight were recorded every two days (Fig. 6A). Figure 6B displays tumor photographs from different treatment groups.

The 100 μg/mL Au@Pd nanozymes-treated group demonstrated the smallest tumor volume and the most effective tumor treatment compared to the control group and other concentrations (Fig. 6C-D). Notably, the body weight of mice in each treatment group remained relatively stable throughout the in vivo treatment period (Fig. 6E), indicating that the biotoxicity of Au@Pd nanozymes towards mice was minimal. In conclusion, the in vivo treatment results suggest that Au@Pd nanozymes exhibit potent tumor growth inhibition capabilities, particularly at a concentration of 100 μg/mL, with negligible biotoxicity. These findings support the potential of Au@Pd nanozymes as a promising and safe therapeutic strategy for treating tumors.

Blood physiology and biochemistry

Blood samples were extracted from the orbital venous plexus of mice in both the experimental and control groups. Subsequently, a comprehensive analysis of the related physiological and biochemical indices associated with kidney and liver function was conducted. The results revealed that the physiological and biochemical markers of renal and liver function, including alanine aminotransferase (ALT) (Figure S5A), aspartate aminotransferase (AST) (Figure S5B), albumin (ALB) (Figure S5C), blood urea nitrogen (BUN) (Figure S5D), creatinine (CREA) (Figure S5E), and total bilirubin (TBIL) (Figure S5F), were all within normal ranges in both the experimental and control groups. This indicates that the treatment with Au@Pd nanozymes did not adversely affect the kidney and liver function of the mice.

HE staining

To study the effects of Au@Pd Nanozymes on key tissues and organs of mouse, we dissected the mouse and removed the main organs such as the heart, liver, spleen, lung, and kidney after the treatment. Hematoxylin-eosin (H&E) staining was performed on the heart, liver, spleen, lung, and kidney of mouse to evaluate the damage of Au@Pd Nanozymes on key tissues of mouse. As shown by HE staining in Fig. 6F and Figure S5G, no obvious tissue damage and inflammatory lesions were observed in the heart, liver, spleen, lung, and kidney of the experimental group and the control group, indicating that Au@Pd Nanozymes had no obvious biological toxic side effects and had good biological safety and could be treated in vivo.

Materials and methods

Materials

$HAuCl_4 \cdot 3H_2O$, $Na_3C_6H_5O_7 \cdot 2H_2O$, Na_2PdCl_4, L-ascorbic acid, and 3',5,5'-tetramethylbenzidine (TMB) were purchased from Sigma-Aldrich (USA); H_2O_2, NaH_2PO_4, and Na_2HPO_4 were purchased from Sinopharm Chemical Reagent Co.,Ltd; DMEM medium, fetal bovine serum, penicillin-streptomycin solution, phosphate-buffered saline, trypsin, chloroform, cell viability assay kit (live/dead staining), and reactive oxygen species assay kit

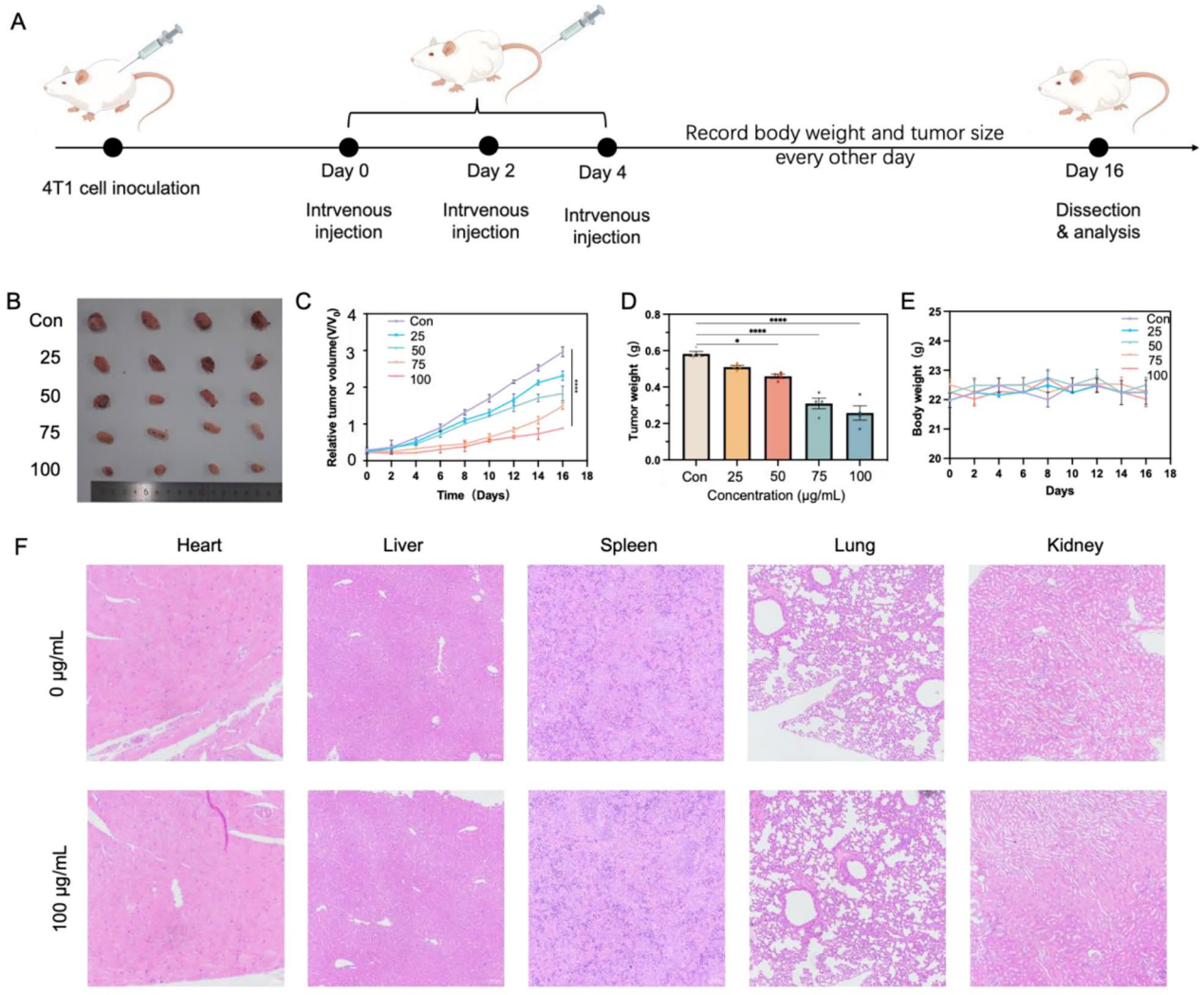

Fig. 6 **(A)** Schematic illustration of the therapeutic procedure ($n = 5$); **(B)** Tumor volume of 4T1 tumor-bearing mouse model in each group after 14 days of treatment; **(C)** Tumor volume change curves of 4T1 tumor-bearing mouse model in each group; **(D)** Tumor weight change curves of each group; **(E)** Weight change curves of 4T1 tumor-bearing mouse model in each group; **(F)** HE staining of heart, liver, spleen, lung, and kidney. $^{*}P < 0.05$; $^{**}P < 0.01$; $^{****}P < 0.0001$

(ROS) were purchased from Dalian Meilun Biotechnology Co., Ltd.; Trizol, RIPA lysis buffer, ECL hypersensitive luminescence reagent, BCA protein concentration assay kit, and PAGE gel preparation kit (10%/12.5%) were purchased from Shanghai Epizyme Biomedical Technology Co., Ltd; PCR primers, reverse transcription kit, SYBR qPCR reagents, and DEPC were purchased from Sangon Biotech (Shanghai) Co., Ltd.; DNA damage assay kit (γ-H2AX immunofluorescence) was purchased from Beyotime Biotechnology; Annexin V-FITC apoptosis detection kit, Cell Counting Kit-8 (CCK-8), HE staining kit, and propidium iodide (PI) solution were purchased from Beijing Solarbio Science & Technology Co., Ltd.; protein markers, Pro-caspase 3 antibody, Pro-caspase 7 antibody, Caspase 3 antibody, Caspase 7 antibody, P53 antibody, Bax antibody, Bcl-2 antibody, Apaf-1 antibody, β-actin antibody, GAPDH antibody, HRP-conjugated goat anti-rabbit IgG, and HRP-conjugated goat anti-mouse IgG were purchased from Abcam (Shanghai) Trading Co., Ltd.

Cell lines and animals

Mouse breast cancer cells (4T1) and mouse mammary epithelial cells (HC11) were purchased from the Chinese National Stem Cell Resource Center. Balb/c female mice (6 weeks old, 20–22 g, SPF) were purchased from Beijing Vital River Laboratory Animal Technology Co., Ltd. All mouse were housed under the same conditions. All animal experiments were conducted in accordance with the guidelines of the Animals Administrative Committee of the Third Affiliated Hospital of Zunyi Medical University.

Synthesis of au NPs and Au@Pd nanozymes

To synthesize the Au@Pd nanoenzyme, start by adding 1 mL of 25 mM $HAuCl_4{\cdot}3H_2O$ solution to a round-bottom flask containing 99 mL of deionized water (ddH2O) and stir thoroughly. Then, introduce 3 mL of $Na_3C_6H_5O_7{\cdot}2H_2O$ solution to synthesize 15 nm Au nanoparticles (Au NPs). Afterward, heat and stir a mixture of ddH_2O, Na_2PdCl_4 solution, and the freshly prepared 15 nm Au NPs. Finally, add 300 μL of L-ascorbic acid solution to obtain the target product, Au@Pd nanoenzyme.

Characterization of Au@Pd nanozymes

The morphological features and particle dimensions of the samples were scrutinized via Transmission Electron Microscopy (TEM) or Scanning Electron Microscopy (SEM). The elemental makeup of the Au@Pd nanozymes was elucidated through Energy-dispersive X-ray spectroscopy (EDS). The Zeta potential of Au NPs and Au@Pd NPs was measured using a nanoparticle size and Zeta potential analyzer.

Stability testing

Samples of the same concentration were dispersed in ddH_2O (10 mL), PBS (10 mL), and high-glucose culture medium (containing 10% fetal bovine serum, 10 mL). After standing, 1 mL aliquots were taken at various time points (Day 1, Day 2, Day 3, … Day 7) for particle size analysis. The particle size changes of Au@Pd NPs in different environments over time were analyzed using DLS (Dynamic Light Scattering).

Hemolysis assay

The biocompatibility of Au@Pd NPs in blood circulation was assessed using a hemolysis assay. Fresh mouse blood was collected and stored in heparinized tubes. The blood was diluted 10 times with sterile PBS and centrifuged at 500 g/min for 5 min at 4 °C to separate and collect red blood cells. Different concentrations (50, 100, 150, 200 and 300 μg/mL) of Au@Pd NPs were incubated with equal volumes of red blood cell suspension at 37 °C for 3 h. PBS solution and ddH2O were used as negative and positive controls, respectively, under the same conditions. After 3 h of incubation, the experimental and control groups were centrifuged at 500 g g/min for 5 min at 4 °C, and the absorbance of the supernatant at 500 nm was measured using a microplate reader to analyze the hemolytic activity of different concentrations of Au@Pd NPs.

Determination of peroxidase activity and kinetics of the enzymatic reaction of Au@Pd nanozymes

HAc-NaAc buffer with different pH (pH=2, 4, 6, 8, and 10), H_2O_2 with different concentrations (initial concentrations of 5 mM, 10 mM, 15 mM, and 20 mM), and TMB solution with different concentrations (initial concentrations of 20 mM, 40 mM, 60 mM, 80 mM and 100 mM) were prepared. By adjusting the single variable and controlling the principle that other variables were unchanged, HAc-NaAc buffer, H_2O_2 solution, Au@Pd Nanozymes solution, and TMB solution were successively added to 1.5 mL EP tubes according to the ratio of "7:1:1:1". The peroxidase activity of Au@Pd Nanozymes under different pH, TMB, H_2O_2, and temperature conditions was analyzed by UV spectrophotometer.

The initial concentration of TMB was fixed to 5 mM, and the initial concentration of H_2O_2 solution was changed (1 mM-100 mM). The absorbance of the reaction system at 652 nm was measured using a UV spectrophotometer. In addition, the initial concentration of H_2O_2 was fixed to 50 mM, and the initial concentration of TMB solution (0.1 mM −10 mM) was changed. The absorbance of the reaction system at 652 nm was measured using a UV spectrophotometer. According to the following equation (kinetic equation, 1.1), the Michaelis-Menten curve was drawn.

$$\nu = \frac{V_{max} \times [s]}{(Km + s)} \tag{1.1}$$

In Eq. 1.1, Km is the Mie constant, Vmax is the maximum reaction rate, and s is the substrate concentration. V is the initial reaction speed, which can be calculated according to the following formula:

$$\nu = \frac{\Delta \ \mathrm{A}}{(\Delta t \times \ \epsilon \ \times \ \iota)} \tag{1.2}$$

In Eq. 1.2, ΔA is the absorbance change of the measured solution at 652 nm, Δt is the initial reaction time (s), ε is the molar absorbance coefficient of the substrate (typically, at 652 nm, ε is 39000 $M^{-1}cm^{-1}$ for oxidized TMB), and l represents the path length (cm) of light propagation in the petri dish.

Cell uptake and ultrathin sections

Incubate 4T1 cells with 50 μg/mL Au@Pd nanozymes for 8 h, collect and precipitate cells, fix overnight with 2.5% glutaraldehyde, dehydrate using graded ethanol, impregnate with resin, embed in resin, thinly section, and apply proper staining for microscopic examination.

Intracellular ROS measurement

Incubate cells with different concentrations of Au@Pd nanozyme solution for 12 hours, then add the DMEM culture medium with 10 mM 2',7'-dichlorodihydrofluorescein diacetate (DCFH-DA) probe and incubate at 37 °C for 30 min to detect ROS.

DNA damage (γ-H2AX immunofluorescence assay)

Following treatment with different concentrations of Au@Pd nanozyme solution, the cells should undergo a series of steps: washing, fixation, immunoblocking, and antibody incubation using a rabbit γ-H2AX monoclonal antibody and an anti-rabbit 488 secondary antibody. Finally, the cells should be stained with DAPI to visualize the nuclei.

Double staining of the live/dead cell assay

Double staining of the live/dead cell assay was carried out using the Calcein-AM/PI Double Stain Kit. 4T1 and HC11 were seeded into a 6-well culture plate. When the cell density reached 80%, the cells were then incubated with Au@Pd nanozyme for 24 h. After washing out the free Au@Pd nanozyme with PBS, the fresh DMEM medium was added. The cells were finally visualized using an inverted microscope.

Flow cytometry analysis cell apoptosis

4T1 and HC11 cells were seeded in 6-well plates and treated with different concentrations of Au@Pd nanozyme solution when the cell density reached 80%. Stain cells with Annexin V-FITC apoptosis detection kit, and analyze cell apoptosis using flow cytometry.

qRT-PCR

Add Trizol to cells with different treatment for facilitates the lysis of cells, then add chloroform and centrifuge to obtain the upper layer solution. Add isopropanol, centrifuge to obtain the precipitate, add ethanol, centrifuge again to obtain RNA. Dilute the RNA with DEPC water and measure absorbance. Use RNA reverse transcription kit to reverse transcribe the obtained RNA into cDNA. Design primers for the target gene, use SYBR Green fluorescent dye for qPCR to determine the expression levels of the target gene.

Western blotting

Add RIPA lysis buffer containing protease inhibitor (PMSF) to cells with different treatment groups, centrifuge to obtain the supernatant containing proteins. Measure protein concentration using a BCA assay kit. Polyacrylamide gel was prepared according to the 12.5%/10% PAGE gel rapid preparation kit. After denaturing the proteins, load them onto a solidified SDS-PAGE gel, run the gel at 75 V for 30 min, then increase the voltage to 150 V. After electrophoresis, perform a protein transfer onto a membrane. The transfer current should be set at 120 mA for 1.5 h. Following the transfer, blocked by adding 5% skim milk, and the blocking solution was discarded after 1 h of incubation at room temperature on a shaker. Incubate the membrane with primary antibodies against the target protein, followed by secondary antibodies. Finally, add chemiluminescent substrate for visualization.

Cell proliferation was detected by CCK-8 assay

CCK-8 was added to the cells in the different treatment groups. According to the experimental design, the absorbance (OD value) was measured by microplate reader at different time points (2 h, 4 h, 6 h, 8 h, 10 h, 12 h, and 24 h), and the experimental data were recorded. The experimental data were calculated by the following formula: cell survival rate (%)=$(OD_{test}\text{-}OD_{blank})/(OD_{control}\text{-}OD_{blank})\times 100\%$.

Tumor model

The cell suspension was diluted to a cell density of 1×10^6 and injected into the right back of balb/c mouse at a dose of 100 μL per mouse. Animal treatment experiments were performed when the tumor volume reached 100 mm^3.

In vivo therapy

4T1 tumor-bearing mouse with tumor volume of 100 mm^3 were randomly divided into 5 groups, with 5 mouse in each group. Depending on the group, 100 μL of various concentrations of Au@Pd nanozymes or PBS buffer was injected through the tail vein. The injections were given every 2 days for a total of 3 injections. Tumor volume, body weight, and mouse body weight were recorded every two days from the time of drug injection. After 16 days of treatment, mouse was sacrificed by cervical dislocation, and hearts, livers, spleens, lungs, kidneys, and tumors were removed. Mouse tissues were fixed in 4% paraformaldehyde for 24 h. The fixed mouse tissues were embedded in paraffin. Paraffin blocks were cut into 5 μm tissue sections using a microtome. Hematoxylin-eosin staining was used. Pictures were taken and recorded by light field microscope. After 16 days of treatment, blood was removed from the mouse using the eye frame blood sampling method. Mouse blood routine kit and blood biochemical kit were used for analysis.

Statistical analysis

All experimental data were repeated three or more times, and each experiment was independent of each other. The data were processed by GraphPad Prism 9 software, and the experimental results were analyzed by Mean±standard deviation (Mean±S.E.M). ns, $P\geq0.05$, no statistical difference between the data was considered. *, $p<0.05$, the data were considered statistically significant. **, $P<0.01$, the data were considered to have a relatively obvious statistical significance. ***, $P<0.001$, the data were considered to be clearly statistically significant.

Discussion

In the long history of human resistance to disease, cancer remains one of the most feared ailments. Currently, cancer is still considered incurable worldwide [42], with approximately 9.7 million cancer-related deaths annually, and the number of new cases and deaths continues to rise [43]. Among these, lung, breast, and colorectal cancers are the top three causes of cancer deaths globally. Clinically, cancer treatment is primarily based on the three pillars of surgery, radiotherapy, and chemotherapy, each with its own advantages and disadvantages [44]. Therefore, there is a growing need for the development of new cancer treatment modalities.

With the development of nanotechnology and biological sciences, new treatment methods have been proposed. For example, photodynamic therapy generates toxic ROS by activating photosensitizers accumulated at the tumor site through light exposure [45], photothermal therapy uses light radiation to generate heat energy to ablate tumors [46], and gas therapy releases toxic gases at the tumor site. Each of these treatments has its own advantages, some of which have been applied or are close to being applied in clinical settings.

In 2007, Chinese scientists successfully synthesized Fe_3O_4 with peroxidase activity, marking the beginning of inorganic nanozymes. Fe_3O_4 nanozymes exhibit peroxidase activity in the acidic tumor microenvironment and can catalyze H_2O_2 to produce biotoxic ROS. ROS are more toxic and destructive than H_2O_2, causing irreversible damage to living organisms, including oxidative damage, nucleic acid mutations, and amino acid conversion, ultimately leading to cell apoptosis [47, 48]. These nanozymes offer the catalytic activity of natural enzymes while overcoming their limitations, such as strict reaction conditions, storage and transportation requirements, poor stability, and high production costs [49, 50]. Since their introduction, synthetic enzymes with bio-catalytic activity have rapidly become a research hotspot.

Subsequently, nanoparticles with various biological enzyme activities in the field of electrochemical immunosensing have been synthesized and reported. Nanozymes mimic peroxidase through two classical pathways: the Fenton reaction, which generates hydroxyl radicals, and the electron transfer pathway [51, 52]. The Fenton reaction pathway primarily involves iron-based nanomaterials that decompose H_2O_2 in the tumor microenvironment into ROS. The electron transfer pathway features nanoparticles like cobalt, which are directly oxidized by electron transfer to the reduced electron acceptor nanozyme, generating ROS (•OH) from H_2O_2. Common types of nanozymes include noble metal nanozymes, metal-organic frameworks (MOFs) [53], metal-based oxides [54], and transition metal-containing biomolecules [55]. Ranji-Burachaloo et al. utilized hydrothermal treatment to reduce NH_2-MIL-88B(Fe) MOFs, partially converting Fe^{3+} to Fe^{2+}. They showed that the reduced MOFs could produce hydroxyl radicals (•OH) through both surface reactions (heterogeneous catalysis) and iron release in acidic environments (homogeneous catalysis) [56]. Consequently, these reduced MOFs generated significantly more •OH radicals compared to other nanoparticles under similar conditions. André and colleagues reported that V_2O_5 nanowires, possessing inherent peroxidase-like (POD) activity, can catalyze the oxidation of POD substrates such as 2,2'-azino-bis(3-ethylbenzothiazoline-6-sulfonic acid) (ABTS) and TMB with the assistance of H_2O_2. Under pH 4.0 conditions, the Km values for ABTS oxidation and H_2O_2 were found to be 2.9 μM and 0.4 μM, respectively. These values are significantly lower than those of the natural enzyme HRP and vanadium-dependent haloperoxidase (V-HPO). Wang et al. synthesized MnPc nanoparticles (MnPcNPs) by the supramolecular assembly of manganese phthalocyanine (MnPc), resulting in size-dependent POD-like activity due to metal–N–C active centers, with optimal-sized nanozymes efficiently accumulating in tumors via the EPR effect and displaying higher catalytic activity in the acidic tumor microenvironment compared to normal tissues, thereby effectively killing cancer cells with minimal side effects [57]. Guo et al. reported a yolk-shell structured spherical nanozyme system composed of a single gold nanoparticle core and a porous carbon shell (Au@HCNs). In an acidic environment, Au@HCNs exhibited enzyme-like activity similar to horseradish peroxidase and oxidase, showing ROS generation capability for tumor eradication [58].

Noble metals like Au, Pd, Pt, Ir, and Rh can form alloys with enhanced catalytic activity compared to single-metal enzymes. Au@Pd nanozymes, formed from gold and palladium, have small diameters and high peroxidase activity, showing great potential for catalytic applications. However, previous studies have focused on their use in biological immune detection and sensing, with limited research on their application in cancer treatment. In this study, Au nanoparticles were prepared via the trisodium citrate reduction method, and Au@Pd nanozymes were synthesized by reducing ascorbic acid and depositing palladium on the Au nanoparticles. These Au@Pd nanozymes exhibited good peroxidase activity and biocompatibility, suggesting significant potential for biomedical and clinical applications. Due to the tumor EPR effect, intravenously injected 20 nm Au@Pd nanozymes efficiently accumulated at the tumor site and exhibited peroxidase activity, consuming H_2O_2 to produce cytotoxic ROS in the acidic tumor microenvironment. The generated ROS disrupted the redox homeostasis of tumor cells, causing DNA damage and apoptosis. Mechanistically, the anti-apoptotic protein Bcl-2 decreased significantly, while pro-apoptotic proteins Bax, caspase 3, caspase 7, and

Apaf-1 increased. Additionally, the expression of the tumor suppressor gene P53 was significantly increased, driven by the ROS generated, which promotes the translation and modification of apoptosis-related genes. This, in turn, enhances the activation and stability of related proteins. We also examined tissue morphology and blood physiological and biochemical status post-treatment in vivo, finding that Au@Pd nanozymes not only demonstrated good biocompatibility but also exhibited high biosafety.

These properties suggest that Au@Pd nanozymes could be developed into an effective therapeutic agent for targeted cancer treatment.For clinical application, we envision several potential uses for Au@Pd nanozymes: (1) Targeted Drug Delivery: Au@Pd nanozymes could be conjugated with tumor-specific ligands or antibodies to enhance their selectivity for cancer cells, minimizing off-target effects and reducing systemic toxicity. (2) Combination Therapy: They could be used in combination with existing chemotherapy or radiotherapy treatments to enhance their efficacy and potentially reduce the required doses of these conventional therapies, thereby mitigating their side effects. (3) Minimally Invasive Treatments: Their use in minimally invasive procedures, such as localized injections directly into the tumor site, could provide a targeted therapeutic approach, reducing the impact on surrounding healthy tissues.

The potential of Au@Pd Nanozyme in clinical applications is promising due to their high catalytic activity, ability to generate ROS in the tumor microenvironment, and good biocompatibility. However, several challenges remain before clinical approval and widespread use can be achieved. (1) Regulatory Approval: Obtaining regulatory approval from agencies such as the FDA and EMA involves rigorous testing for safety, efficacy, and quality. This process can be time-consuming and costly. (2)Scalability: Industrial-scale production of Au@Pd nanozymes must ensure consistent quality and activity. Developing cost-effective and reproducible synthesis methods is essential for commercial viability. (3)Long-Term Safety: Long-term biocompatibility and toxicity studies are needed to assess the potential side effects of Au@Pd nanozymes in humans, particularly their accumulation and clearance in the body. (4)Targeted Delivery: Ensuring efficient and targeted delivery to tumor sites while minimizing off-target effects remains a significant challenge. Further research on optimizing the delivery mechanisms is required. (5)Clinical Trials: Extensive preclinical studies followed by multi-phase clinical trials are necessary to establish the therapeutic benefits and safety profile of Au@Pd nanozymes in cancer treatment.

In summary, while Au@Pd Nanozyme show great potential in cancer therapy, overcoming these challenges will be critical for their translation from the laboratory to the clinic.

Conclusion

In summary, we have successfully synthesized Au@Pd nanozymes by trisodium citrate reduction and ascorbic acid reduction followed by deposition of metal palladium. Due to the EPR effect, Au@Pd nanozymes accumulate at tumor sites for catalytic therapy. Au@Pd nanozymes had good physiological stability in aqueous solution, PBS solution, and DMEM solution, and the particle size was 20 nm. In the acidic tumor microenvironment, Au@Pd nanozymes showed good peroxidase catalytic activity and good ROS generation ability by catalyzing H_2O_2. The generated ROS induces overexpression of tumor apoptosis-related proteins and further leads to cell apoptosis. In vitro cell experiments showed that Au@Pd nanozymes were able to be efficiently internalized by tumor cells and catalyze ROS production from H_2O_2. Fluorescence imaging showed that Au@Pd nanozymes catalyze the generation of large amounts of ROS, causing DNA damage and cell death, demonstrating good catalytic therapeutic ability. In vivo studies showed that Au@Pd nanozymes exhibited a good tumor inhibition effect after successfully entering tumor cells. Therefore, our work provides an effective approach to nanozyme-based catalytic therapy.

Abbreviations

ALT	Alanine aminotransferase
Apaf-1	Apoptotic protease activating factor-1
AST	Aspartate Transaminase
Au	Aurum
Bax	BCL2-Associated X
BCA	Bicinchoninic Acid
Bcl-2	B-cell lymphoma-2
BMN	Blood Mrea Nitrogen
CCK-8	Cell Counting Kit-8
CDT	Chemodynamic Therapy
Crea	Creatinine
DAPI	4′,6-diamidino-2-phenylindole
DLS	Dynamic Light Scattering
DMEM	Dulbecco's modified eagle medium
ECL	Enhanced chemiluminescence
EDS	Energy dispersive spectrometer
ELSA	Enzyme linked immunosorbent assay
FBS	Fetal bovine serum
GAPDH	Glyceraldehyde-3-phosphate
HAc	CH3COOH
HE	Hematoxylin and Eosin staining
PBS	Phosphate buffered saline
Pd	Palladium
PDT	Photodynamic Therapy
PI	Propidium iodide
POD	Peroxidase
Pt	Platinum
WB	Western Blot
TMB	Tetramethylbenzidine

Supplementary Information

The online version contains supplementary material available at https://doi.org/10.1186/s12967-024-05631-8.

Supplementary Material 1

Acknowledgements
We also thank Figdraw (www.fgdraw.com) for the assistance in creating Scheme (Fig. 1A).

Author contributions
ML: Formal analysis, writing-original draft and editing; YMW: Drawing fgures and conceptualization; Sorting of articles and resources; Technical support; FKZ: Investigation and validation; Mapping and sorting tables; Funding acquisition and supervision; JB: Funding acquisition, Writing—review and editing; PW: Project administration and funding acquisition. All authors reviewed the manuscript. The author(s) read and approved the fnal manuscript.

Funding
This work was supported by the Transfer Payment Project of Science and Technology Department of Sichuan Province (22ZYZF-S-02), the Fundermental Research Fund for Universities of Yunnan Province (202101BA070001-099).

Data availability
The datasets generated and/or analysed during the current study are not publicly available due [REASON WHY DATA ARE NOT PUBLIC] but are available from the corresponding author on reasonable request.
Author contact: 19707763798@163.com.
The reason why the data of the research paper is not disclosed is that the next research mechanism is still involved. In addition, all the data of the research paper are the original data of the research subject, and the data set is not involved or used from any public platform.

Declarations

Ethics approval and consent to participate
All animal experiments were conducted in accordance with the guidelines of the Animals Administrative Committee of the Third Affiliated Hospital of Zunyi Medical University.

Consent for publication
Not applicable.

Competing interests
The authors state that there are no conflicts of interest to declare.

Received: 14 June 2024 / Accepted: 18 August 2024
Published online: 02 September 2024

References

1. Brandeis M. A primer to proliferation. Nat Cell Biol. 2001;3(8):E187–187.
2. Pérez E, Bergmann A. Intercellular cannibalism fuels tumor growth. Cell Death Differ. 2017;24(5):759–60.
3. Shewach DS, Kuchta RD. Introduction to Cancer Chemotherapeutics. Chem Rev. 2009;109(7):2859–61.
4. Ferlay J, Colombet M, Soerjomataram I, et al. Cancer statistics for the year 2020: an overview. Int J Cancer. 2021;149(4):778–89.
5. Fabbro M, Colombo PE, Leaha CM, et al. Conditional probability of survival and prognostic factors in long-term survivors of high-Grade Serous Ovarian Cancer. Cancers. 2020;12(8):2184.
6. Foster M, Niedzwiedz CL. Associations between multimorbidity and depression among breast cancer survivors within the UK Biobank cohort: a cross-sectional study. BMC Cancer. 2021;21(1):650.
7. Moshiri K. AABH (aspartyl [asparaginyl] β-hydroxylase) as a serum biomarker for breast cancer. J Clin Oncol. 2020;38(5):2–2.
8. Jaiswal P, Tripathi V, Nayak A, et al. A molecular link between diabetes and breast Cancer: therapeutic potential of repurposing incretin-based therapies for breast Cancer. Curr Cancer Drug Targets. 2021;21(10):829–48.
9. Zarshenas MM, Mohammadi-Bardbori A. A medieval description of metastatic breast cancer; from Avicenna's view point. Breast. 2017;31:20–1.
10. Srivastava A. We have travelled a long way! Indian J Surg. 2021;83(2):269–72.
11. Rossi L, Materazzi G, Bakkar S, et al. Recent trends in Surgical Approach to thyroid Cancer. Front Endocrinol. 2021;12:699805.
12. Wang Y, Shen J, Gu P, et al. Recent advances progress in radiotherapy for breast cancer after breast-conserving surgery: a review. Front Oncol. 2023;13:11955266.
13. Iram S, Zahera M, Wahid I, et al. Cisplatin bioconjugated enzymatic GNPs amplify the effect of cisplatin with acquiescence. Sci Rep. 2019;9(1):13826.
14. Ruggiero A, Rizzo D, Catalano M, et al. Hypersensitivity to Carboplatin in Children with Malignancy. Front Pharmacol. 2017;8:201.
15. Takenaka T, Inoue T, Miyazaki T, et al. Klotho suppresses the renin-angiotensin system in adriamycin nephropathy. Nephrol Dialysis Transplantation. 2017;32(5):791–800.
16. Zhang Y, Wang CX, Huang SW. Aggregation-Induced Emission (AIE) Polymeric Micelles for Imaging-guided photodynamic Cancer therapy. Nanomaterials. 2018;8(11):921.
17. Jiang Q, Gao X, Zhang W, et al. Recent progress in metal-organic framework-based sonosensitizers for sonodynamic tumor therapy. Biomater Sci. 2023;11(13):4452–70.
18. Gao L, Zhuang J, Nie L, et al. Intrinsic peroxidase-like activity of ferromagnetic nanoparticles. Nat Nanotechnol. 2007;2(9):577–83.
19. Lu C, Zandieh M, Zheng J, et al. Comparison of the peroxidase activities of iron oxide nanozyme with DNAzyme and horseradish peroxidase. Nanoscale. 2023;15(18):8189–96.
20. Alizadeh N, Salimi A. Multienzymes activity of metals and metal oxide nanomaterials: applications from biotechnology to medicine and environmental engineering. J Nanobiotechnol. 2021;19(1):26.
21. Singh S. Antioxidant nanozymes as next-generation therapeutics to free radical-mediated inflammatory diseases: a comprehensive review. Int J Biol Macromol. 2024;260(1):129374.
22. Sheng J, Wu Y, Ding H, et al. Multienzyme-like Nanozymes: Regulation, Rational Design, and application. Adv Mater. 2024;36(10):2211210.
23. Chen M, Zeng G, Xu P, et al. How do enzymes 'Meet' nanoparticles and nanomaterials? Trends Biochem Sci. 2017;42(11):914–30.
24. Shoeibi S, Mozdziak P, Golkar-Narenji A. Biogenesis of Selenium nanoparticles using Green Chemistry. Top Curr Chem (Cham). 2017;375(6):88.
25. Feng J, Yao T, Ma Z. Recent advances of peroxidase-active nanozymes in electrochemical immunoassays. Sens Diagnostics. 2023;2(4):781–91.
26. Xu J, Xu Y, Bu XH. Advances in emerging crystalline porous materials. Small. 2021;17(22):e2102331.
27. Cheng X, Zhou X, Zheng Z, et al. Construct efficient substrate transport and catalytic sub-nanochannels in metal-organic framework-based nanozymes for boosting peroxidase-like catalytic activity. Chem Eng J. 2022;430:133079.
28. Yan X, Zhao H, Shi X, et al. Dual function of 4-Aminothiophene in surface-enhanced Raman scattering application as an Internal Standard and Adsorbent for Controlling au Nanocrystal morphology. ACS Appl Mater Interfaces. 2023;15(10):13427–38.
29. Mochizuki C, Nakamura J, Nakamura M. Effects of Au States in Thiol-Organosilica nanoparticles on enzyme-like activity for X-ray sensitizer application: focus on reactive Oxygen species Generation in Radiotherapy. ACS Omega. 2023;8(10):9569–82.
30. Chang M, Hou Z, Wang M, et al. Single-atom pd nanozyme for ferroptosis-boosted mild-temperature Photothermal Therapy. Angew Chem Int Ed Engl. 2021;60(23):12971–9.
31. Tian X, Chen Z, Yang L, et al. Low-temperature photothermal therapy platform based on pd nanozyme-modified hydrogenated TiO(2). ACS Appl Mater Interfaces. 2023;15(38):44631–40.
32. Li D, He X, Su M, et al. One-pot synthesis of hierarchical concave tetrapod pd nanocrystals and their electrocatalytic properties. RSC Adv. 2017;7(60):37938–42.
33. Chen J, Tang Y, Lin Y, et al. Dual-coordinated atomically dispersed pt nanozymes evoke efficient pyroptosis for cancer immunotherapy. Chem Eng J. 2024;483:149312.
34. Najafi L, Bellani S, Castelli A, et al. Octapod-shaped CdSe nanocrystals hosting pt with high Mass activity for the hydrogen evolution reaction. Chem Mater. 2020;32(6):2420–9.
35. Mu S, Deng Y, Xing Z, et al. Ir cluster-anchored MOFs as peroxidase-mimetic nanoreactors for diagnosing hydrogen peroxide-related biomarkers. ACS Appl Mater Interfaces. 2022;14(51):56635–43.
36. Song G, Shao X, Qu C, et al. A large-pore mesoporous Au@Pt@Rh trimetallic nanostructure with hyperthermia-enhanced enzyme-mimic activities

for immunomodulation-improved tumor catalytic therapy. Chem Eng J. 2023;477:147161.
37. Marzun G, Levish A, Mackert V, et al. Laser synthesis, structure and chemical properties of colloidal nickel-molybdenum nanoparticles for the substitution of noble metals in heterogeneous catalysis. J Colloid Interface Sci. 2017;489:57–67.
38. Ji Y, Hou M, Zheng Y, et al. A 3D network structured reduced graphene oxide/PtRu alloyed composite catalyst in-situ assembled via particle-constructing method. Colloids Surf a. 2019;561:292–300.
39. Feng K, Wang G, Wang S, et al. Breaking the pH limitation of Nanozymes: mechanisms, methods, and applications. Adv Mater. 2024;36(31):e2401619.
40. Sheng J, Wu Y, Ding H, et al. Multienzyme-like Nanozymes: Regulation, Rational Design, and application. Adv Mater. 2024;36(10):e2211210.
41. Jiang B, Duan D, Gao L, et al. Standardized assays for determining the catalytic activity and kinetics of peroxidase-like nanozymes. Nat Protoc. 2018;13(7):1506–20.
42. Regassa H, Sourirajan A, Kumar V, et al. A review of Medicinal plants of the Himalayas with anti-proliferative activity for the treatment of various cancers. Cancers (Basel). 2022;14(16):3898.
43. Rumgay H, Arnold M, Ferlay J, et al. Global burden of primary liver cancer in 2020 and predictions to 2040. J Hepatol. 2022;77(6):1598–606.
44. Zheng PP, Li J, Kros JM. Breakthroughs in modern cancer therapy and elusive cardiotoxicity: critical research-practice gaps, challenges, and insights. Med Res Rev. 2018;38(1):325–76.
45. Liu J, Zhai F, Zhou H, et al. Nanogold Flower-inspired Nanoarchitectonics enables enhanced light-to-heat Conversion ability for Rapid and targeted chemo-photothermal therapy of a Tumor. Adv Healthc Mater. 2019;8(8):e1801300.
46. Wang Y, Barhoumi A, Tong R, et al. BaTiO(3)-core Au-shell nanoparticles for photothermal therapy and bimodal imaging. Acta Biomater. 2018;72:287–94.
47. Abbasi A, Pakravan N, Hassan ZM. Hyaluronic acid optimises therapeutic effects of hydrogen peroxide-induced oxidative stress on breast cancer. J Cell Physiol. 2021;236(2):1494–514.
48. Kamil A, Khan MA, AAsim M, et al. Detection of ROS and translocation of ERP-57 in apoptotic induced human neuroblastoma (SH-SY5Y) cells. BIOCELL. 2019;43(3):167–74.
49. Wang C, Ren G, Yuan B, et al. Enhancing enzyme-like activities of prussian Blue Analog Nanocages by Molybdenum Doping: toward Cytoprotecting and Online Optical Hydrogen Sulfide Monitoring. Anal Chem. 2020;92(11):7822–30.
50. Liu Q, Zhu X, Zhong L, et al. Recent advances in the applications of nanozymes for the efficient detection/removal of organic pollutants: a review. Environ Science: Nano. 2022;9(4):1212–35.
51. Chen L, Yang Z, Qian J, et al. Interaction between Organic compounds and Catalyst Steers the Oxidation Pathway and mechanism in the Iron Oxide-based Heterogeneous Fenton System. Environ Sci Technol. 2022;56(19):14059–68.
52. Wan K, Jiang B, Tan T, et al. Surface-mediated production of Complexed •OH radicals and Fe = O species as a mechanism for Iron Oxide Peroxidase-like Nanozymes. Small. 2022;18(50):e2204372.
53. Guan X, Ge X, Dong H, et al. Ultrathin 2D Pd/Cu single-atom MOF nanozyme to synergistically overcome Chemoresistance for Multienzyme Catalytic Cancer Therapy. Adv Healthc Mater. 2023;12(30):e2301853.
54. Dubey P, Sertorio M, Takiar V. Therapeutic advancements in metal and metal oxide nanoparticle-based radiosensitization for Head and Neck Cancer Therapy. Cancers. 2022;14(3):514.
55. Feng J, Yang X, Du T, et al. Transition Metal High-Entropy Nanozyme: Multisite Orbital Coupling Modulated High-Efficiency peroxidase mimics. Adv Sci. 2023;10(33):e2303078.
56. Ranji-Burachaloo H, Karimi F, Xie K, et al. MOF-Mediated Destruction of Cancer using the cell's own hydrogen peroxide. ACS Appl Mater Interfaces. 2017;9(39):33599–608.
57. Wang J, Gao S, Wang X, et al. Self-assembled manganese phthalocyanine nanoparticles with enhanced peroxidase-like activity for anti-tumor therapy. Nano Res. 2022;15(3):2347–54.
58. Fan L, Xu X, Zhu C, et al. Tumor Catalytic-Photothermal Therapy with Yolk-Shell Gold@Carbon Nanozymes. ACS Appl Mater Interfaces. 2018;10(5):4502–11.

Publisher's note